# Sensitivity of multiscale large Eddy simulations for wind power calculations in complex terrain

Giorgia De Moliner [a], Paolo Giani [b,1], Giovanni Lonati [a], Paola Crippa [b,*]

[a] Department of Civil and Environmental Engineering, Politecnico di Milano, Piazza Leonardo da Vinci 32, Milan, 20133, Italy
[b] Department of Civil and Environmental Engineering and Earth Sciences, University of Notre Dame, 156 Fitzpatrick Hall of Engineering, Notre Dame, 46556, IN, USA

GRAPHICAL ABSTRACT
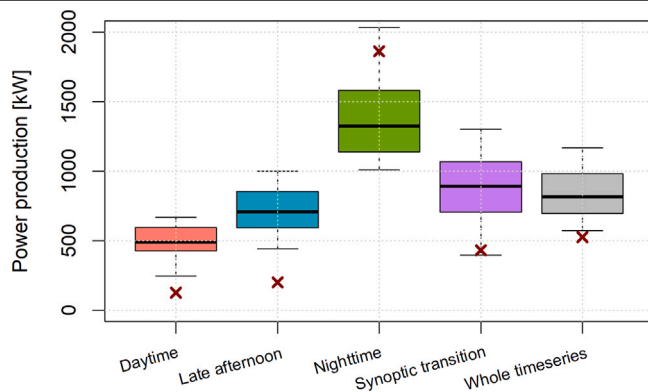
ARTICLE INFO

ABSTRACT

Coupling Large Eddy Simulations (LES) with Numerical Weather Prediction (NWP) models has promising applications for wind energy. Regional climatology, optimal siting of wind turbines as well as short term wind energy forecasts can be improved by considering all the energetic scales of atmospheric motions. However, the complexity of NWP-LES coupled simulations introduces challenges and uncertainties that need to be addressed. This study focuses on understanding the relative importance of different factors and assumptions in NWP-LES calculations for wind energy applications. Using a recent large ensemble of LES simulations driven by NWP boundary conditions over the complex terrain of the Perdigão area, our analysis reveals significant discrepancies in wind power estimates across ensemble members, particularly over hilltops. Depending on the model configuration and the coupling technique, instantaneous predictions can be as sensitive as 800 kW for a 2 MW wind turbine, in terms of ensemble standard deviation. On multi-day time averages, the model sensitivity is in the order of 150 kW. We further analyze the main factors that lead to the observed model sensitivity. Results from a four-way analysis of variance identify topography and land use datasets as the primary drivers of variability, for time averaged estimates. The temporal analysis shows strong inter-daily variability and the importance of turbulence modeling and the coupling techniques for instantaneous predictions. Overall, most of the sensitivity is observed during day-to-night and synoptic transitions. By understanding the relative importance of different factors, future model development and applications can be informed to enhance the accuracy and reliability of wind energy assessments.

* Corresponding author.
  E-mail addresses: giovanni.lonati@polimi.it (G. Lonati), pcrippa@nd.edu (P. Crippa).
[1] Present address: Department of Earth, Atmospheric and Planetary Sciences, Massachusetts Institute of Technology, Cambridge, 02139, MA, USA

1. Introduction

The imperative need of transitioning current energy systems, heavily reliant on fossil fuels, to renewable and carbon-neutral energy sources is motivated by the need of addressing pressing environmental and societal challenges, including climate change, public health, energy security, and economic development. Many countries, including the United States, China and European Union member states, have set ambitious net-zero emissions targets, necessitating significant transformations, such as transitioning to renewable energy sources and increasing energy efficiency [1,2]. Wind energy is a crucial component of these plans due to its cost-effectiveness and minimal environmental impact throughout its lifecycle. Decades of scientific advancements and technological progress have propelled wind energy to become a mainstream source of electricity, accounting for nearly 7% of the world's total electricity generation [3]. Current studies suggest that wind energy alone could fulfill the world's entire energy demand by 2030 [4,5]. Nevertheless, more research and innovations are critical to meeting these expectations, as a widespread use of wind energy will require technology to be pushed into uncharted territories, both scientifically and engineering-wise [6,7]. Additionally, continuous advancements are essential to ensure the cost-effectiveness and competitiveness of wind energy in the market [4,5]. Veers et al. [6] identified three primary challenges in wind energy research that must be tackled to enable an extensive and cost-effective utilization of wind energy: (i) a comprehensive understanding of the atmospheric flow dynamics within wind farms' operational zone, (ii) the aerodynamics and structural dynamics of larger wind turbines, both onshore and offshore, and (iii) a collaborative integration of wind farms into the future electricity grid. The present study contributes to the first objective by investigating what is the sensitivity of wind energy calculations with nested and realistic Large Eddy Simulations (LES).

Quantifying and predicting wind speeds at turbine hub height requires understanding atmospheric dynamics and microscale flow properties within the planetary boundary layer (PBL), a task that is particularly challenging in regions of complex terrain [8], namely areas characterized by irregular topography and land use. Several studies have investigated microscale flows in complex terrain via high resolution numerical simulations, in idealized settings (e.g., with LES [9]) or via lower resolution Reynolds-Averaged Navier–Stokes (RANS) methods for Numerical Weather Prediction (NWP) applications, in realistic settings [10]. Accurate simulations of processes at such fine spatial scales also require acknowledgment that the microscale flow is influenced by larger mesoscale conditions, thus developing full-physics coupled meso- to micro-scale simulations (i.e., multiscale simulations) is critical to obtain a realistic model output [11,12]. The meso- to micro-scale coupling, also referred to as multiscale simulations, is particularly challenging, as current meso- and micro-scale models rely on fundamentally different assumptions to resolve turbulence processes. Mesoscale models are based on the RANS approach, where unsteady mean properties of the flow are of interest and turbulent vertical transport in the PBL is completely parameterized with 1D PBL schemes. Conversely, microscale LES models, applied at finer resolution (i.e., tens of meters), directly resolve the energy-containing turbulent eddies and parameterize the effect of the unresolved subgrid scales (SGS) on the mean flow. Major uncertainties and challenges still remain as how to couple meso- to micro-scale simulations and to properly simulate phenomena at gray zone (GZ) or Terra Incognita resolutions [13], which occur at around 1 km and for which assumptions from SGS parameterizations and 1D PBL schemes are violated [14]. As a result, unrealistic flow structures may be simulated if traditional closure techniques are not revised [15,16]. However, it is of high interest to perform simulations at gray zone resolutions, as they dynamically inform finer nests and are critical to a number of different applications. While recent studies have explored new approaches to overcome these

difficulties [17–21] and improve the accuracy and efficiency of multi-scale model runs (e.g., [12,22–24]), a comprehensive understanding on the subject is still elusive [25,26].

The growing expansion in computational resources has allowed full-physics, online coupling between mesoscale weather simulations and microscale simulations for wind energy purposes [27–29], where the coarsest LES domain is forced by realistic and time varying lateral boundary conditions generated by the parent simulation. Large-scale tendencies are dynamically integrated in high-resolution simulations, thus overcoming several idealizations in canonical LES that relies on steady-state forcing [30]. Realistic inhomogeneous terrain can also be incorporated, which overcomes limitations of downscaling attempts with doubly-periodic boundary conditions that integrate unsteady large-scale tendencies [31,32]. The full online coupling approach is particularly important to study transient phenomena (e.g., frontal passages [33], thunderstorm outflows, baroclinic systems, low-level jets) and changes in atmospheric stability associated with the diurnal–nocturnal cycle [34], topography-induced flow [35], and to link site-specific wind conditions to the long-term climatology of the area [34]. The latter plays a key role in providing reliable predictions of the annual energy potential of wind farms, thus reducing financial risks [36], particularly in regions of complex terrains. Short-term wind energy forecasts can also benefit from LES coupled with mesoscale simulations [37,38]. However, multiscale simulations are still in their early stage, are highly complex and require many input parameters and assumptions, potentially leading to large uncertainties in their output. In this study, we leverage a recently performed numerical experiment including 36 full-physics multiscale simulations, which specifically investigate PBL dynamics and modeling challenges at gray zone resolutions [39], and bring a novel perspective on the impact of numerical modeling choices and the representation of all relevant scales for wind energy applications. Our goal is to explore the sensitivity of wind energy estimates, derived from a unique ensemble of runs spanning the full range of scales, from the meso- to the micro-scale (LES runs), and quantify their uncertainty and sensitivity to a range of input modeling settings. Specifically this work aims to:

1. Characterizing the time-resolved sensitivity and uncertainty of wind power production estimates with multiscale numerical simulations, for an isolated 78 m wind turbine in complex terrain (Perdigão field site);
2. Characterizing the spatial distribution of the sensitivity of multiscale simulations for wind energy purposes, to further elucidate the role of complex terrain;
3. Providing a benchmark study that can serve as a reference for wind energy assessments performed in areas of complex terrain with multiscale simulations.

The remainder of the paper is organized as follows. In Section 2.1 we present the numerical simulation ensemble, followed by the methodology for the sensitivity analysis (Sections 2.2 and 2.3). The results from the sensitivity analysis are laid out in Section 3, where we address and discuss the temporal (Section 3.1) and the spatial (Section 3.2) distribution of variability within the ensemble. Thereafter, we investigate the sensitivity of power production in Section 3.3. Finally, in Section 4, we present the main findings, draw overall conclusions and outline potential areas for future research.

2. Materials and methods

2.1. Numerical meso- to micro-scale simulations

This work is based upon a recent ensemble of multiscale simulations [39] over the Perdigão field site (Portugal), which is characterized by two parallel ridges and a small valley in between, in an area that is approximately 6x6 km² [40,41]. The two parallel ridges are about 1.5 km apart and are roughly 4 km long and 550 m high at their
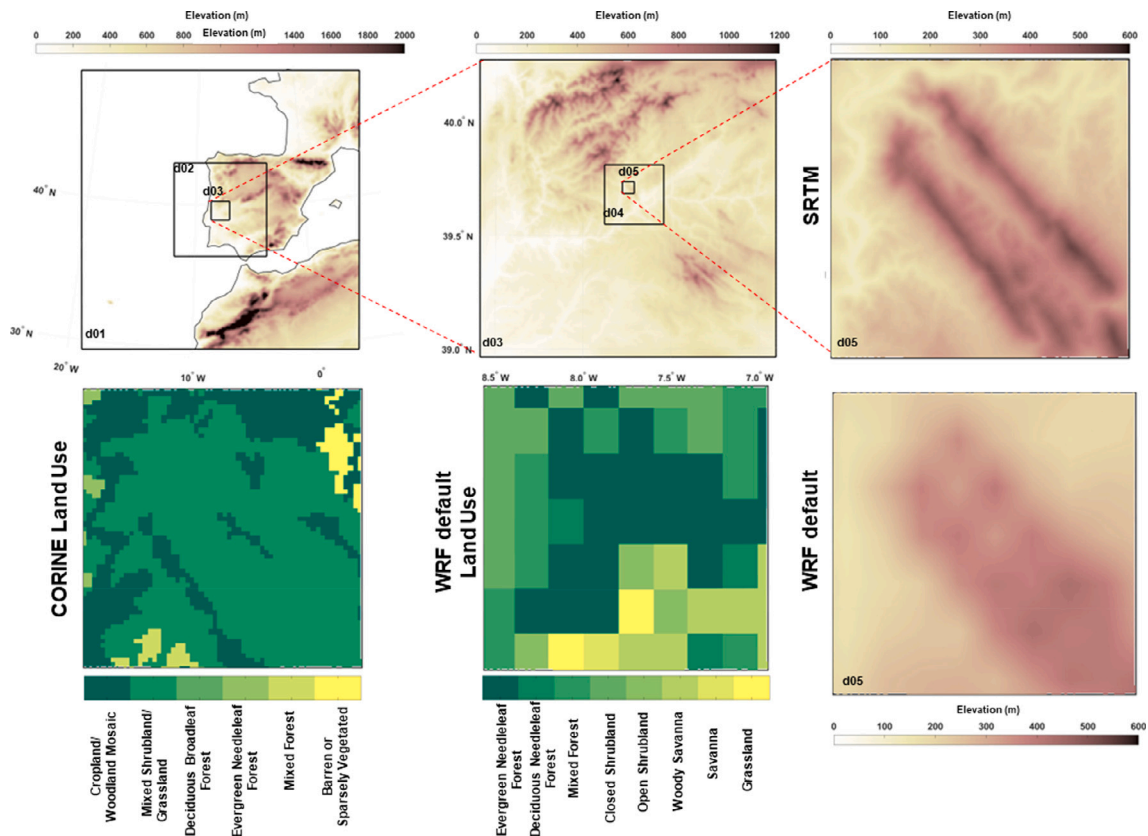
Fig. 1. Five nested domain configuration (d01–d05) for the WRF and WRF-LES simulations analyzed in this work (first row). The color shading indicates the SRTM (Shuttle Radar Topography Mission) 30 m resolution topography expressed as meters above sea level. The second row shows the land use categories according with the different datasets used (i.e., CORINE and WRF default-MODIS21), as well as the coarse, default, topography in WRF, for d05.

summit. Relevant experimental details [40] of the campaign and other modeling work over the Perdigão valley [41–44] can be found in recent literature. An in-depth description of the ensemble is presented in [39], whereas here we report the main features of such simulations.

The 36 simulations ensemble members were generated with the Weather Research and Forecasting (WRF) model version 4.4 [45] and its WRF-LES component, and comprise five nested domains. The grid spacing of the five domains spans from 11.25 km in the outermost domain (d01) to 30 m in the innermost one (d05) as displayed in Fig. 1, while the vertical discretization is fixed in the first three domains and more refined in d04 and d05, with a vertical spacing of about 20 m in the first 100 m, as described in Table 1. The WRF code solves the compressible, non-hydrostatic Euler equations on the Arakawa-C grid with hybrid, terrain-following, dry hydrostatic pressure as the vertical coordinate [46]. The default WRF time discretization is the time-split third-order Runge Kutta (RK3) scheme with a fixed time step for meteorologically-relevant modes and smaller time steps for acoustic and gravity-wave modes. No random perturbations were used to trigger turbulence (e.g., the Cell Perturbation Method proposed by [47]) since the surface heterogeneity in our case study provides natural perturbations that trigger local circulation and are more substantial than imposing artificial perturbations on the model.

The general circulation in the outermost domain is solved with a mesoscale turbulence parameterization (1D PBL scheme) while the flow in the innermost domain, that interacts with the double-ridge topography, is solved with microscale LES closures. The difference across the 36 configurations lies in four different input factors. Specifically, the ensemble runs include (i) different topography and land use datasets in the d03, d04 and d05 (Table 1) domains (*Topography*), (ii) different initial and lateral boundary conditions for the outermost domain (*LBCs*), (iii) different turbulence closures in the intermediate

Table 1

Five nested domain configuration applied in the ensemble runs. The second column indicates the number of grid cells simulated, the third column the horizontal resolution, the fourth column the approximate vertical resolution at the bottom of the boundary layer, and the last column the time step applied at each resolution.

Domain	$N_x \times N_y \times N_z$	$\Delta x = \Delta y$	Δz_S	Δt
d01	$196 \times 196 \times 77$	11250 m	36 m	75 s
d02	$196 \times 196 \times 77$	3750 m	36 m	25 s
d03	$196 \times 196 \times 77$	750 m	36 m	5 s
d04	$196 \times 196 \times 91$	150 m	24 m	1 s
d05	$196 \times 196 \times 109$	30 m	12 m	1/5 s

gray zone domains (*GZ treatment*) and (iv) different SGS models for the LES innermost domain (*SGS-LES*). Two different options are used for *Topography*, and include the default WRF coarse datasets (around 900 m in resolution) and tailored fine datasets from NASA's Shuttle Radar Topography Mission (SRTM [48]) for topography and the Coordination of Information on the Environment (CORINE) for land use [49], that have 30 m and 100 m resolution, respectively. We use both the default WRF static datasets and ad-hoc high-resolution datasets (SRTM and CORINE) to test the sensitivity of the model to these settings and underscore the importance (or lack thereof) of going beyond WRF default settings and implementing ad-hoc datasets for high-resolution WRF applications. Three choices are used for *LBCs*, including the Global Data Assimilation System (GDAS) final analysis [50], the high-resolution operational data from the European Centre for Medium-Range Weather Forecast (HRES-ECMWF [51]) and ECMWF's ERA5 reanalysis [52]. Boundary conditions are updated every 6 h for HRES-ECMWF and GDAS, whereas they are updated hourly for ERA5-driven simulations. Three choices are considered for *GZ treatment*: a traditional 1D PBL scheme (The Yonsei University Scheme, YSU [53]), the scale-aware

version of the YSU (Shin-Hong [20]), that introduces scaling factors to account for partially resolved turbulence, and Zhang's 3D blending closure [17], that was also designed to be scale-adaptive but also calculate horizontal fluxes. All three options (a PBL scheme, scale-aware schemes and 3D closures) have been used in recent literature [25], and they differ in the way subgrid turbulent fluxes of heat, momentum and moisture are computed. Finally, two options are tested for *LES-SGS*, the Turbulent Kinetic Energy (TKE) closure of Deardorff [54] and the deformation-based Lilly–Smagorinsky closure [55,56]. The values for the Smagorinsky constant and the TKE coefficient are 0.25 and 0.15, respectively. The ensemble includes every possible combination of options for the four input factors resulting in $2 \times 3 \times 3 \times 2 = 36$ simulations.

The simulations cover four days during the Intensive Operation Period of the Perdigão field experiment, from May 19th 2017, 00 UTC to May 23rd 2017, 00 UTC. Note that the local time is UTC+1 during the simulated episode, and results with a temporal component are reported in UTC. During the simulation days, no precipitation, but a mixture of clear sky days and high and medium clouds are observed [40,41]. The simulated period starts from relatively high pressure conditions linked to fair weather, and the flow over the double ridge is mostly dynamically-driven. During the night of May 20 and May 21, a low pressure system, stronger winds aloft, and high clouds, reach the domain from the South-West. By late May 21 and May 22, weaker synoptic winds reach the Perdigão area, allowing for more local thermodynamically induced valley–ridge circulations.

2.2. Four-way analysis of variance

The goal of this work is to disentangle the effect and the relative importance of the four different input factors described in Section 2.1 on time-varying wind power estimates at a specific point in space, where a 78 m tall wind turbine is located, as well as across the simulated spatial domain. We focus on the innermost domain (d05), discretized at 30 m resolution and simulated with 36 different configurations of WRF-LES. To evaluate the sensitivity of the dataset to various input factors, we perform a four-way Analysis of Variance (ANOVA [57]) which identifies the factors with greatest impact on the variability across the ensemble members by decomposing the variance.

To assess both the spatial and temporal variability of the model output, we conduct two separate analyses. The spatial analysis covers the entire innermost domain, while the temporal analysis focuses only on the turbine site. Both analyses examine the relationship between wind speed at 78 m and power production. Wind speed at 78 m is linearly interpolated from the two closest vertical grid points at each time step. Further, we conduct the sensitivity analysis for both the entire simulated time period and four specific sub-periods of interest: (i) *daytime* (12–15 UTC), which features a fully developed convective boundary layer (CBL); (ii) *late afternoon* (16–20 UTC), which represents the transition period from daytime to nighttime; (iii) *nighttime* (00–03 UTC, May 19–21), when a stable boundary layer conditions prevails; and (iv) a period characterized by a change in synoptic conditions (May 21, 12 UTC to May 22, 06 UTC), when both the prevailing wind direction and wind speed vary significantly (*synoptic transition*).

Here we first introduce the fundamental concepts of a one-way ANOVA, and then generalize it to a four-way version, required to explore the model sensitivity to the four perturbed input factors. Each factor comprises K number of levels or groups, which correspond to the input options discussed in Section 2.1 (i.e., $K = 2$ for *Topography*, $K = 3$ for *LBCs*, $K = 3$ for *GZ* and $K = 2$ for *LES-SGS*). In each group there are N runs, which in our ensemble is constant across groups within the same factor, for a total of KN runs. The purpose of a one-way ANOVA is thus to test if runs from several groups in a factor have the same mean. Let x_{ij} be the simulated value x for run $j = 1, \ldots, N$ in group $i = 1, \ldots, K$, so for example x_{14} is the fourth run in the first group. If, for instance, we were testing the model sensitivity to only the *LBC* factor
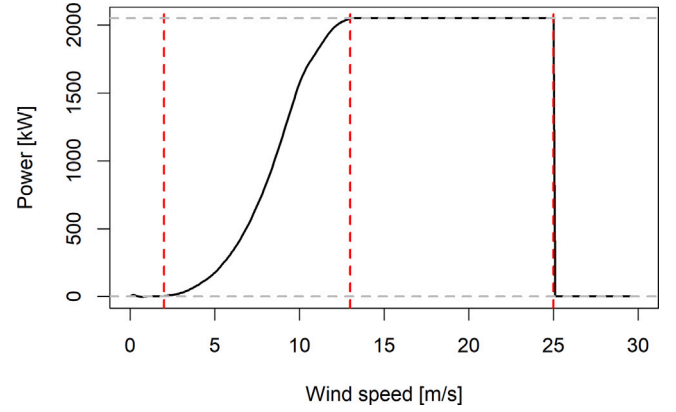

Fig. 2. ENERCON-2 MW wind turbine power curve [58]. Dashed red lines represent the cut-in speed, rated speed and cut-off values, from left to right.

the three groups would have been GDAS, ERA5, HRES-ECMWF, and so x_{14} would be the wind values from the fourth run that uses GDAS as *LBCs*.

A one-way ANOVA tests if the group means of x are different by partitioning the total variance into the variation between groups and the variation within a group. Formally, we perform the following decomposition:

$$x_{ij} = \overline{\overline{x}} + (\overline{x_i} - \overline{\overline{x}}) + (x_{ij} - \overline{x_i}), \quad \forall i = 1, \ldots, K, j = 1, \ldots, N \quad (1)$$

where $\overline{\overline{x}}$ is the average across all KN runs and $\overline{x_i}$ is the mean of group i. Thus, the term $(\overline{x_i} - \overline{\overline{x}})$ indicates the variation of the group i mean from the overall mean, while $(x_{ij} - \overline{x_i})$ indicates the variation of the runs within each group from their group mean. According to the decomposition of Eq. (1), measures of dispersion within the ensemble can be computed as follows:

$$s^2_{explained} = \frac{1}{KN} \sum_i \sum_j (\overline{x_j} - \overline{x})^2 = \frac{1}{N} \sum_j (\overline{x_j} - \overline{x})^2 \quad (2)$$

$$s^2_{residual} = \frac{1}{KN} \sum_i \sum_j (x_{ij} - \overline{x_j})^2 \quad (3)$$

The explained variance ($s^2_{explained}$) indicates the extent to which group means match the grand mean, thus large values of $s^2_{explained}$ indicate large departures among the means of each group. Accordingly, it shows how much of the ensemble variability is explained by differences in *LBC*. The residual variance, instead, quantifies differences within each group and consequently computes the amount of variability introduced by any other factor. A simple rearrangement of Eq. (1) provides the mean to decompose the total variance into the sum of the previous two quantities:

$$s^2_{total} = \frac{1}{KN} \sum_i \sum_j (x_{ij} - \overline{x})^2 \equiv s^2_{explained} + s^2_{residual} \quad (4)$$

A four-way ANOVA is a generalization of a one-way ANOVA and calculates the corresponding $s^2_{explained}$ for each input factor and allocates the remaining variance to $s^2_{residual}$. Therefore, the decomposition of total variance for a multi-way ANOVA can be expressed as follows:

$$\sum_{m=1}^{M} s^2_{explained,m} + s^2_{residual} = s^2_{total} \quad (5)$$

where M is the number of factors (i.e. M = 4 in our case). We use the software *R* to compute the four-way ANOVA.

2.3. Power curve and wind energy production

The time-resolved ANOVA focuses on a single grid point, selected by the shortest Euclidean distance to an ENERCON E-82 E1 wind turbine,
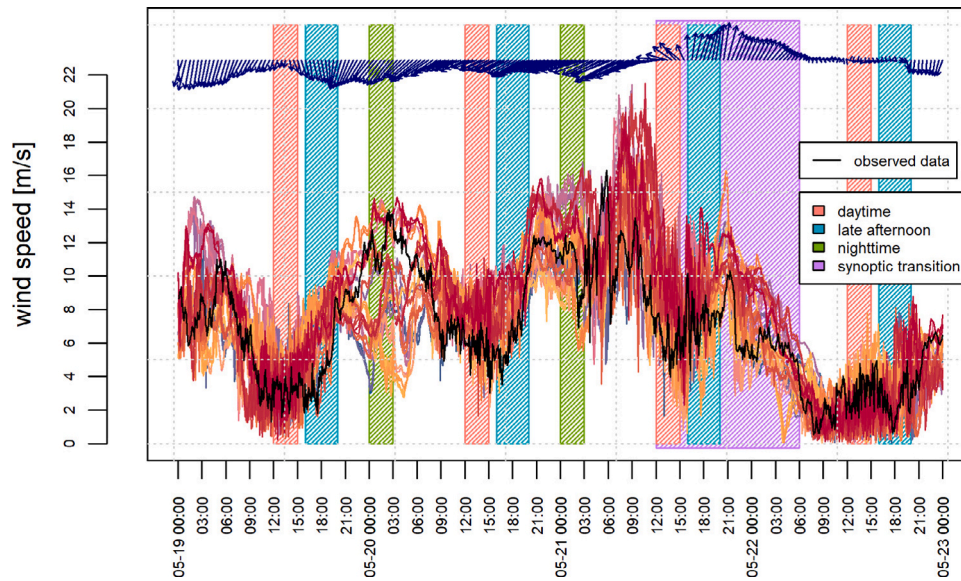
Fig. 3. Temporal variability of five minutes averaged simulated wind speed (m s^{-1}) at the turbine location at hub height (i.e., 78 m) across the 36 ensemble members. Observations are in black and the arrows on top represent the hourly mean direction the wind is blowing to and the length of the bar is proportional to the mean wind speed across the ensemble runs. The vertical bars indicate the hours used in the analyses over specific period of interest defined in Section 2.2 (i.e., *daytime, late afternoon, nighttime* and *synoptic transition*).
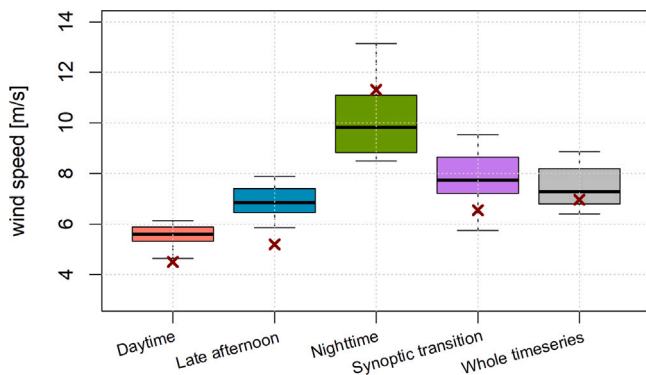

Fig. 4. Time-averaged wind speed at the turbine height and location for each sub-period of interest and for the whole simulated period. Each box refers to the variability across the 36 ensemble members. Each whisker extends to the furthest data point in the ensemble that is within 1.5 times the interquartile range (IQR). Red crosses show observations at *tse04* averaged in time during the same time periods.

78 m tall and with a rated power of 2 MW that has been in operation since 2007, located on the south-west ridge (39.708N, 7.745W). The power curve in Fig. 2 is used to estimate wind power production based on the simulated wind speeds at turbine hub height. The cut-in wind speed for power to be generated is about 2 m s^{-1}. After that threshold is met, wind power increases approximately with the third power of wind speed up to the rated speed at 13 m s^{-1}. Further increases in wind speed will not affect power production, which remains constant at the wind turbine rated power (2 MW). However, if the wind speed exceeds the cut-off value (25 m s^{-1}), the turbine is not allowed to deliver power to prevent excessive stress on the structure. It is worth noting that internal and external factors that also lead to different energy yield rates [59] are not taken into account in our wind power estimates. Finally, it should be noticed that our simulations do not include an actuator disk wind turbine model [60] to avoid introducing further sources of uncertainty. Thus, the simulated downwind flow at the turbine location is not impacted by the presence of the actual turbine.

3. Results

3.1. Temporal variability of wind speed at the turbine site

Here we present five-minutes averaged simulated wind speed data extracted from the 36 ensemble members at the turbine location at hub height (Fig. 3). Although a full model evaluation is beyond the scope of this study, we briefly compare the simulated wind speeds with the observed five-minutes averages at the closest meteorological mast that includes near hub-height measurements (100 m), to assess model's skill in capturing key dynamic processes at the site that are relevant to this work. The meteorological mast was located on the South-West ridge (39.706N, 7.744W) and its code for the Perdigão field campaign is *tse04*. The observations indicate a clear diurnal cycle, with wind speeds decreasing during convective daytime conditions and increasing at night, a trend that is generally captured by all model runs. During the synoptic transition on late May 21 and May 22, a notable shift in the typical diurnal cycle is observed. Specifically, the wind direction shifts from ENE to SSW, the wind speed drops, and the typical nighttime increase in wind speed is not observed (top of Fig. 3). This perturbation is driven by weaker winds aloft, as well as by a change in wind direction that precludes the typical wind speed amplification observed on the second/downwind ridge, where the turbine is located, when there is a northeasterly flow.

The median value of wind speed averaged over the whole four-day period matches the observed data within 0.5 m s^{-1}, as shown in Fig. 4 (in gray). However, our multiscale runs tend to overestimate the median wind speed by approximately 1.5 m s^{-1} during daytime and late afternoon and to underestimate it by a similar amount during nighttime. The different model setups adopted do not have a significant impact on the discrepancies across the ensemble members, as highlighted by the small spread between the 1st and 3rd quartiles of approximately 0.5 m s^{-1} during daytime and late afternoon. During these time periods, the model consistently exhibits a positive bias against observations. The variability across the ensemble members also varies through time, with the largest variability occurring during nighttime and synoptic transition periods. For example, on May 22, during the synoptic transition characterized by a shift to a southerly flow, the wind speed is weaker on average compared to the previous nights and similar to the day–night transition. However, the spread across the ensemble
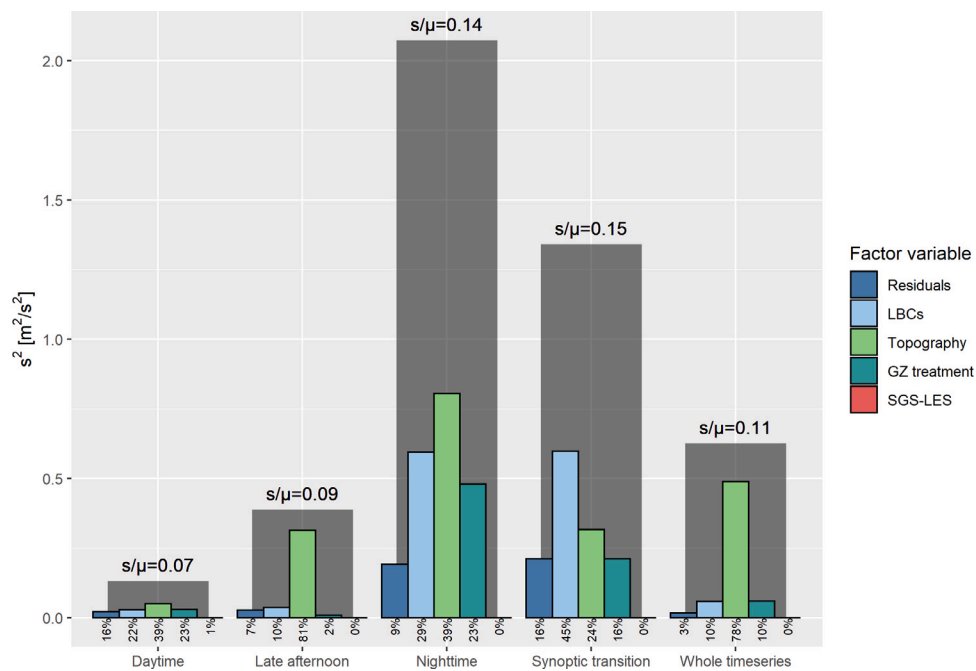
Fig. 5. Decomposition of total variance (in gray) of time-averaged wind speed, among factor variables. Wind speeds have been simulated at the turbine site and at 78 m. On top of the gray bars, is the coefficient of variation (i.e., standard deviation divided by the mean) is shown, while at the bottom of each colored bar, the percentage of explained and residual variance is displayed.

runs is larger during this period (Fig. 4), indicating higher uncertainty in the model's ability to accurately capture the wind speed variability. These results suggest that the nighttime and stratified flow conditions are the most challenging for the model to capture, and that different parameterizations/forcing play a key role in generating uncertainty across runs. Modeling challenges in simulating stratified flows over complex terrain are well established and have been identified in other recent studies performed with coarser grid spacing (1–3 km) [61–65].

To quantify the role of each of the four factors under examination in driving discrepancies across the ensemble members an ANOVA is performed on wind speeds at hub height averaged either over the whole timeseries or over the individual four sub-periods. Fig. 5 illustrates the total variance (in gray) and how it is broken down across factors, according to the methodology described in Section 2.2. With the exception of the synoptic transition, the characterization of topography is the primary factor contributing to 40%–80% of wind speed variability across runs. The coarser terrain dataset (i.e., the WRF default) considerably smooths the terrain and leads to a three-dimensional hill rather than a double ridged topography, which will impact the simulated mountain–valley flow and thus generate discrepancies across the runs. The fine and coarse land use datasets also differ in terms of surface roughness thus further contributing to generate differences. Thus, a careful selection of the static dataset adopted in WRF is critical to properly estimate near-surface wind speeds using realistic LES, particularly over complex terrain, in accordance with [43,66].

During daytime and nighttime periods, the LBCs and the GZ treatment also contribute to the spread, each by more than 20%, whereas their impact is much less relevant during other time periods (i.e., day–night transition and whole-day averages). As far as the synoptic transition is concerned, the LBCs factor mostly drives discrepancies in wind speeds by contributing to 45% of total variance. Here, the elsewhere dominant topography only accounts for 24% of the variability across runs. This is likely due to the mesoscale nature of the phenomena driving PBL dynamics under changes of synoptic conditions, as during late May 21 and May 22. Therefore, when simulating synoptic transition episodes emphasis should be placed on how initial and later boundary conditions for the outermost domain are represented. The temporal

frequency of LBCs updates appears here to be particularly relevant. The SGS model adopted is generally the least relevant factor, contributing to about 1% of the total variability across runs.

Finally, the decomposition of variance performed on the five-minutes data over the whole time series indicates some inter-daily variability (Fig. 6). Occasionally, a single factor may persistently prevail over the others for a certain time frame (e.g., gray zone treatment on the first night). However, a consistent daily pattern cannot be inferred. On May 19 and May 20, the largest total variance is found at night, consistently with the results in Fig. 4. Other patterns are identified on May 21 and May 22, where high and low variances are constantly observed throughout the two days, respectively. On May 22, none of the four factors is found to dominate, which can be interpreted in light of the overall small variance associated with the low simulated wind speeds. As discussed earlier, the change in synoptic conditions might be responsible for this pattern, which is also reflected in the large variance explained by *LBC* between 12 and 18 UTC on May 21. The five minutes analysis allows to further identify interesting phenomena that are not revealed by the time-averaged analysis. For example, during the night between May 19 and May 20, the vast majority of the spread within the ensemble can be traced back to how turbulence has been modeled at gray zone resolutions. Conversely, as previously shown in Fig. 5, nighttime averaged variances show that topography is the leading factor in explaining the model sensitivity. This analysis thus reveal that, while a certain factor may drive the variability across runs for time averaged values, other factors may dominate when high-frequency data are analyzed.

In conclusion, our results suggest that when a time aggregated analysis is of relevance, as in the cases of optimal turbine siting and regional climatology, topography and land use datasets are the leading factors in determining the *time-averaged* wind speeds. The reason is that lower or higher surface roughness, for instance, consistently lead to higher and lower wind speed, respectively, biasing the time averages. On the contrary, when a prediction with a short time resolution is of interest, as in the case of hourly forecasts necessary to match the energy demand, different results should be expected.
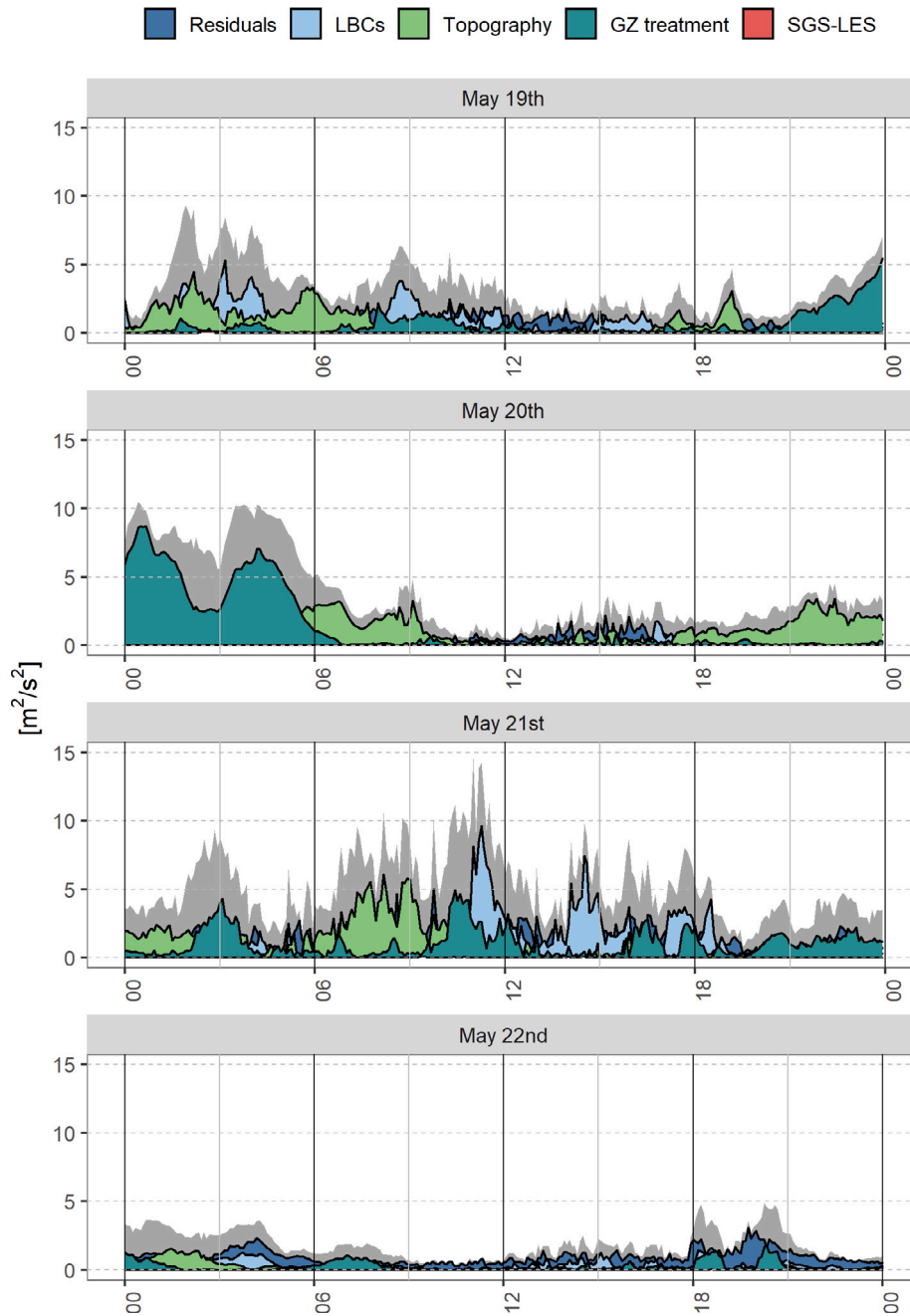
Fig. 6. Decomposition of total variance [m² s⁻²] of wind speed at 78 m above ground at the turbine site on each simulated day. The total variance is reported in gray.

3.2. Spatial sensitivity of wind speed to model setup

In this section, results of the sensitivity analysis performed over the entire innermost domain are presented. The goal is to characterize the spatial distribution of the sensitivity of multiscale simulations of wind speed and thus investigate the role and the consistency in space of each of the four factors under examination. To this end, a four-way ANOVA is performed in each grid point on time-averaged wind speeds at 78 m. Fig. 7 shows the variance explained by each factor variable, on a logarithmic scale. Each row represents the five periods of interest over which time-averaged wind speeds are computed.

Regardless of the sub-period, results show a significant influence of the topography and land use datasets on the simulated wind speeds, especially on the two parallel ridges and on the deepest section of the in-between valley (upper-left area), where the total variance itself is higher compared to the rest of the domain. As also highlighted

in Section 3.1, different accuracies in characterizing the topography of the area leads to significant differences in the simulation of the mountain–valley flows and thus generated discrepancies within the ensemble. On the contrary, in all sub-periods and over the whole spatial domain, the model is rather insensitive to the LES SGS model, as also found in the time-resolved analysis. During nighttime and the synoptic transition, other factors gain importance, as shown in Fig. 8. These effects are particularly visible on the second ridge downwind (the SW and NE ones, respectively for *Nighttime* and *Synoptic transition*) where discrepancies among runs are higher, as well as in the flat region further downwind (respectively, lower-left and upper-right corners). Furthermore, it is of interest to note that in the deepest region of the valley it is again only topography that leads to substantial differences in wind speeds within the ensemble. The flat region upwind (in Fig. 7, northeast and southwest corners for all subperiods and for synoptic transition, respectively) which are not influenced by the presence of
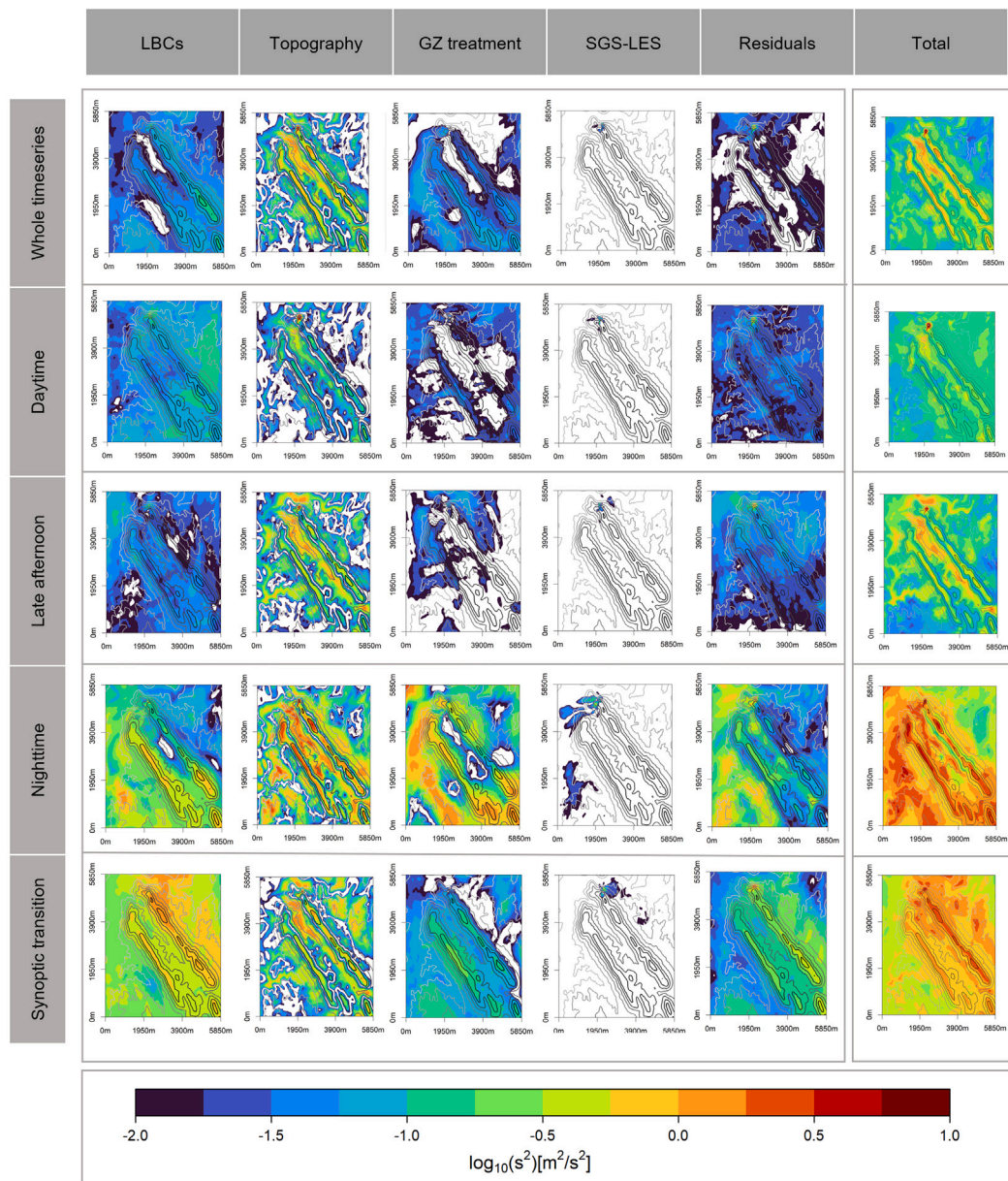
Fig. 7. Variance explained (m² s⁻²) by each factor over the whole time series and the individual four periods of interest. The last column shows the part of variance not explained by the adopted ANOVA model. Note the $\log_{10}$ scale of the colorbar. In white, variances of less than 0.01 m² s⁻² are shown. X and Y axis are displayed as distances in meters from the most South-West point of the domain (39.685N, 7.774W). The topography contours (30m-SRTM) are showed in gray colorscale.

the ridges indicate lower sensitivities to the majority of the factors (white, blue and green in Fig. 7) and generally a high agreement across simulations as indicated by a general variability of ±0.3 m s⁻¹ among time-averaged wind speed. Given the limited impact of the ridges on the flow in these areas, results in this region may be informative of sensitivity in flat terrains in general.

Under both synoptic transition and nighttime conditions, when variance is relatively high, a portion of total variance is explained by the residuals. As interactions of all orders between additive terms are not included in the ANOVA presented here, the residuals account for them all and thus for the variability introduced by varying two or more factors simultaneously (as shown in the Methods Section 2.2).

ANOVA with first-order interactions has shown prevalence of interactions of topography, LBCs, and GZ treatment as the most relevant ones (not shown). Lastly, an area of numerical instabilities is observed at the northwest edge of the northern ridge, which is most likely a result of the limited capability of WRF hybrid hydrostatic pressure

terrain-following coordinates to accurately simulate very steep slopes close to numerical boundaries (not shown). This is reflected in the non-negligible portion of variance explained by the LES SGS model in that area, suggesting that different subgrid scale models play a role in interacting with the numerical instabilities created by the fast horizontal and vertical velocities in the steep region of the domain (slope angles greater than 45 degrees). Note that off-centering (forward centering $\tau = 0.4$ [67,68]) is used in the implicit time integration of the vertical momentum equation and the geopotential equation (in the acoustic loop) to damp the vertically-propagating acoustic modes and keep the model stable [39].

In summary, when simulating multi-day averaged wind speeds in complex terrain through multiscale simulations, as well as for daytime and late afternoon sub-periods, the elevation mapping and the land use dataset chosen for the site mostly drive the spread within the ensemble. This holds particularly true over ridges and in the valleys in between. With the exception of LBCs in the daytime, the other
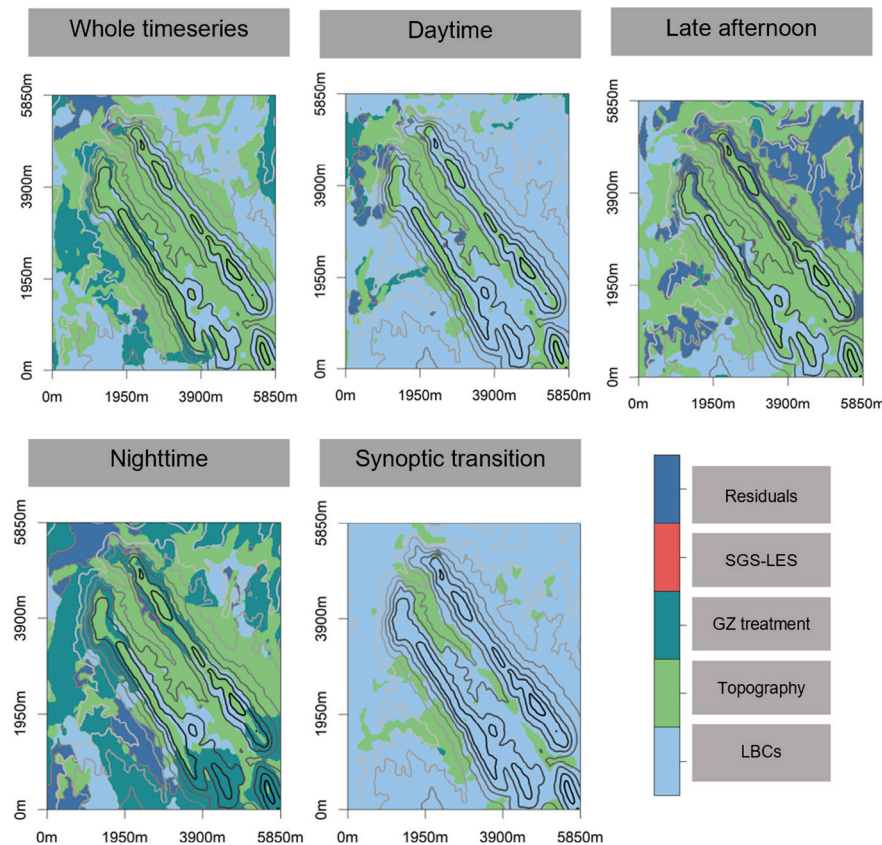
Fig. 8. Factors explaining most of the variance at each location and time period. X and Y axis are displayed as distances in meters from the most South-West point of the domain (39.685N, 7.774W).

Table 2

Mean values of the variance explained by each factor when simulating wind speed in different time frames (columns 1-5, in percentage) computed over the whole innermost domain. Residuals account for interactions of all orders. Results are shown as percentages of the spatial mean of total variance (m^2 s^{-2}), which is presented in the last column.

	LBCs	Topography	GZ	SGS-LES	Residuals	Total (m^2 s^{-2})
Whole Period	19.5	60.9	12.7	0.29	6.69	0.219
Daytime	42.9	29.5	10.8	0.46	16.4	0.160
Late afternoon	14.5	62.9	5.54	0.30	16.7	0.234
Nighttime	19.4	32.9	32.3	0.32	15.0	1.142
Synoptic transition	55.4	21.6	7.81	0.21	15.0	0.848

factors under examination do not significantly influence wind field simulations. When nighttime and synoptic transition wind speeds are of interest, instead, also the resolution and temporal forcing of global dataset, as well as the representation of turbulence in the gray zone are of relevance in dictating discrepancies in wind speed estimates. Table 2 summarizes these findings. In each entry, mean values of the variance explained by each factor computed over the whole innermost domain are given. Results are presented as percentages of the mean value of total variance, which is instead displayed in the last column in m^2 s^{-2}.

3.3. Sensitivity of wind power production at the turbine site

We now examine how various modeling approaches affect the power generation predictions, with specific focus on the wind turbine location on the southern ridge of the Perdigão domain. Although we can apply our approach to any point within the study area, we choose this site as a demonstration of a realistic application with an existing wind turbine. In addition, measurements at *tse04* enable the comparison of power production estimates obtained from the WRF-LES

simulated wind speeds with those from the actual observations. Fig. 9 illustrates the fluctuation of wind power generation over time among the ensemble members and in comparison with the measurements.

Similarly to the wind speed in Fig. 3, the power production peaks over nighttime and is lowest during daytime periods, with a mean of 1390 kW and 490 kW, respectively. While the mean wind speed over the entire time period analyzed only slightly overestimates observations (see Fig. 3), the model bias for the mean power production is much larger, 840 kW from the model versus 525 kW from observations. Namely, a 37% average power difference is found for the ensemble mean, while the same wind speed bias in percentage was only 7%. The imbalance increases in all sub-periods, although it is during daytime that the highest difference is found, as the discrepancy between observations and ensemble mean is equal to 74% of latter (19% for wind speed). This can be explained by considering that the power production generally scales with the cube of the wind speed (see Fig. 2), thus biases in wind speeds may be significantly amplified when estimating wind power. As expected, the variability among the ensemble members is also amplified in relation to the wind speeds, as demonstrated in Fig. 10. The coefficient of variation (CV), displayed on top of each bar in both Figs. 5 and 11, is used to quantify and compare such differences.

Values of CV (i.e., the standard deviation between ensemble members divided by the ensemble mean) are twice or even three times (during daytime) higher compared to their wind speed equivalents. In the case of wind power, the greatest variability within the ensemble is found during the period of synoptic transition (coefficient of variation equals to 0.31), although the greatest variation in absolute terms occurs in nighttime as its standard deviation is 305 kW, against the 270 kW of synoptic transition. For comparison, the average electricity power consumption for a single American household is approximately 1.2 kW, from U.S. Energy Information Administration [69] estimates — which implies that different model predictions would be different by an
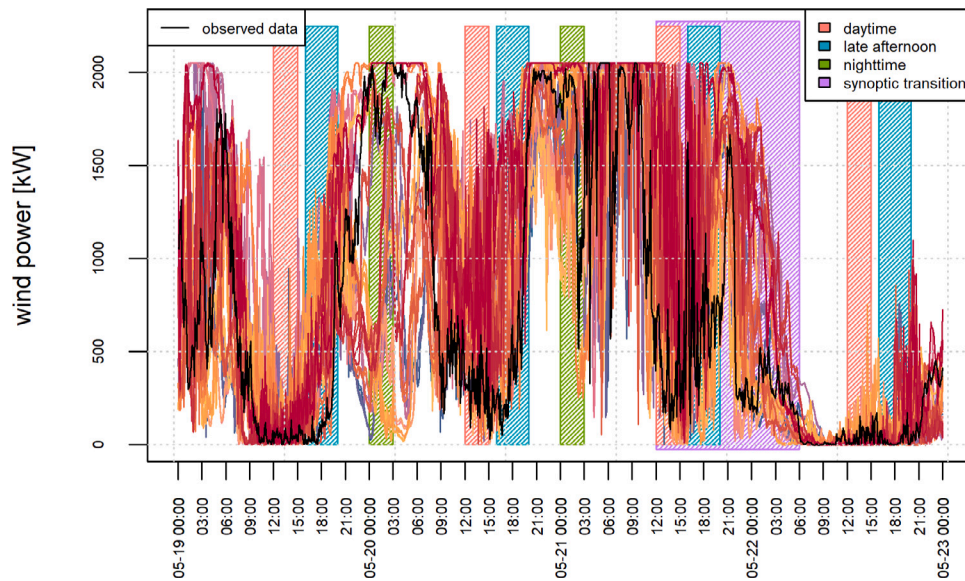
Fig. 9. Power production estimates [kW] for an ENERCON-2 MW turbine derived from the simulated five-minutes averaged wind speeds at 78 m at the location of the existing wind turbine on the southern ridge. The different lines represent the wind power generated using wind speeds from different ensemble members. The black line refers to the power estimated from the observed wind from a nearby meteorological mast (*tse04*), at near hub height (100 m).
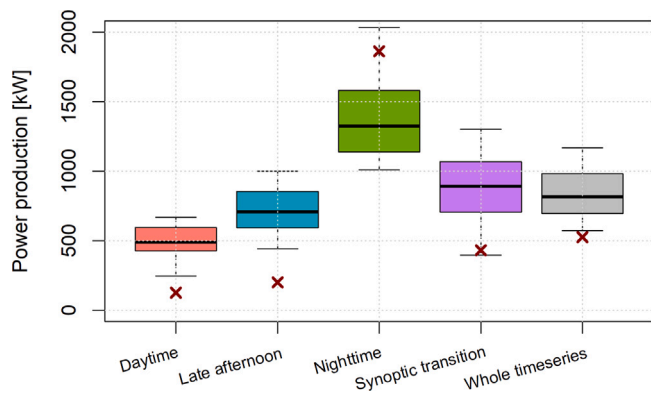

Fig. 10. Time-averaged wind power at the turbine height and location for each sub-period of interest and for the whole simulated period. Each box refers to the variability across the 36 ensemble members. Each whisker extends to the furthest data point in the ensemble that is within 1.5 times the IQR. Red crosses show wind power computed from the observed time-averaged wind speeds.

amount that, for a single turbine, could power about 250 households, during nighttime. Therefore, the ensemble power variability across the ensemble is significant, highlighting the importance of further constraining multiscale LES calculations to have a highly accurate and reliable simulation tool for realistic applications. During the daytime and late afternoon time periods, as well as for averages over the whole four-day period, discrepancies between ensemble members are halved if compared to other periods. However, they are still significant and not negligible.

Here we present results from the ANOVA decomposition of variance performed over power productions estimated from the simulated winds at the turbine site and averaged either over the whole timeseries or over individual sub-periods of interest. Fig. 11 displays similar patterns to the ones of wind speeds (Section 3.1, Fig. 5). When the whole time series and late afternoon are analyzed, topography resolution still appears to be a dominant factor in explaining the variability in power production across runs, with a contribution of around 70%. During synoptic transition, as it was in the previous analysis, the model is most

sensitive to LBCs, whose different characterizations account for 44% of total variance. Yet, in other sub-periods some discrepancies in sensitivity patterns compered to wind speed analyses can be noticed. Given the characteristic power production curve (detailed in Section 2.3), whenever the input wind speeds are either below 2 m s⁻¹ (cut-in speed) or exceed 13 m s⁻¹ (rated speed), the power production saturates, as depicted in Fig. 9. Therefore, when all simulations exhibit wind speeds either below 2 m s⁻¹ or above 13 m s⁻¹, an increase in wind speed does not result in an increase in power generation, and the spread among the simulated wind speeds leads to equal power production estimates, pushing variance to zero, and making it insensitive to all factors. Similarly, when only certain runs of the ensemble simulate wind speeds above or below these thresholds, the relative importance of each factor may vary compared to previous sensitivity analysis on wind speeds. This is the case of nighttime and daytime sub-periods. As captured in Fig. 3, indeed, during the first two nights certain runs simulate winds faster than 13 m s⁻¹, while during May 19 and daytime hours of May 22 wind speeds occasionally drop below 2 m s⁻¹. Consequently, main explaining factors of total variance for wind power differ from the wind speed ones. In particular, in both nocturnal and diurnal hours, the effect of topography is reduced, in favor of LBCs (52%) and GZ treatment (45%), respectively for daytime and nighttime. In conclusion, under specific wind conditions (i.e., wind speeds of about 2 or 13 m s⁻¹), improvements of the input features highlighted by our wind speed sensitivity analysis may not necessarily enhance power production estimates, and vice versa.

Similar conclusions can be drawn for ANOVA performed on five-minutes power production simulations, whose decomposition of variance is presented in Fig. 12. Generally, similar sensitivity patterns to the wind speed analysis can be seen. However, 'deformations' due to the characteristic power curve of wind turbine are still visible. An illustrative case is set by May 21. On the one hand, during the early hours when wind speed are consistently above 13 m s⁻¹ in some simulations, decomposition of variance of wind power returns an altered sensitivity pattern if compared to previous results on wind speed, characterized by the absence of predominance of any factor. On the other hand, after 12 UTC, when wind speed starts dropping and the simulated wind direction begins to shift from ENE to SSW starting synoptic transition, the same pattern of the wind speed analysis can be detected, characterized by the dominance of LBCs effects, overtaken
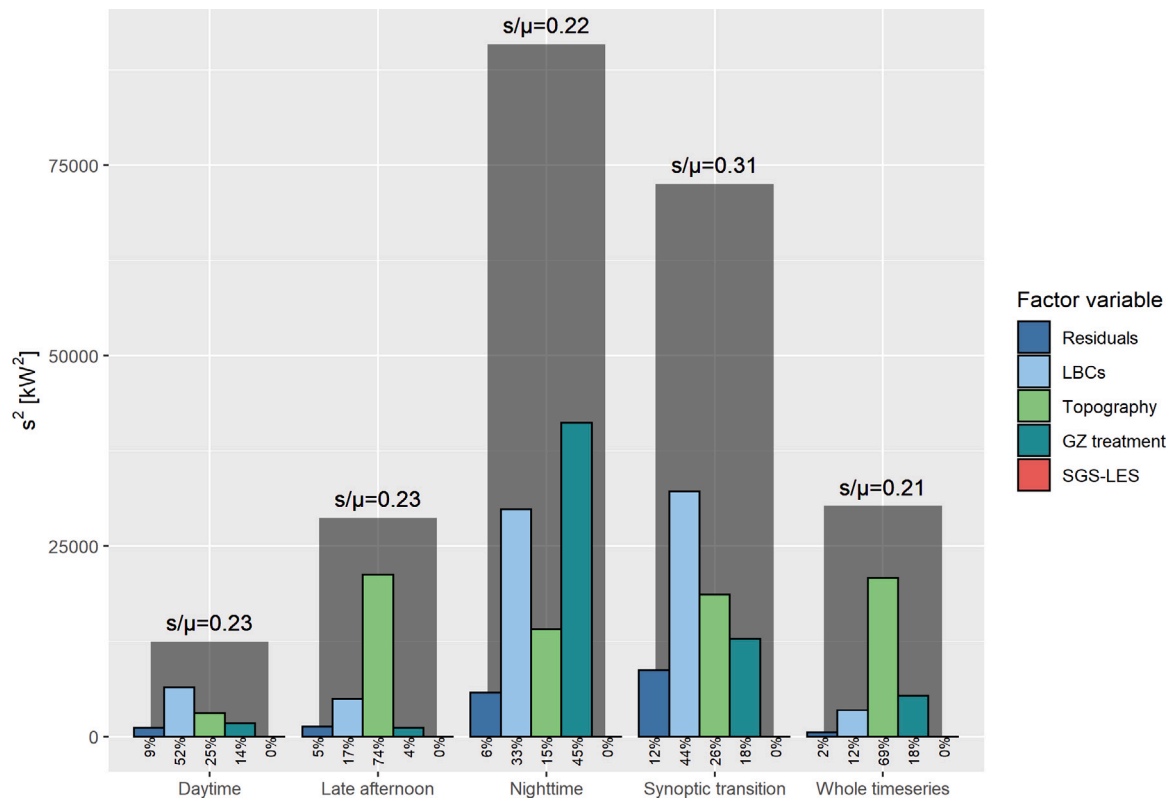
Fig. 11. Decomposition of total variance (in gray) of time-averaged power productions, among factor variables. Wind speeds have been simulated at the turbine site and at 78 m above ground. On top of the gray bars, the coefficient of variation (i.e., standard deviation divided by the mean) is shown, while at the bottom of each colored bar, the percentage of explained and residual variance is displayed.

by the gray zone treatment as the sun sets. The only difference is the magnitude of the curves, here amplified by the characteristic cubic shape of power curve when wind speeds are well between the range 2–13 m s^{-1}.

4. Discussion and conclusions

Multiscale modeling tools have the capability to simulate atmospheric motions across a broad range of spatio-temporal scales, covering almost all energetic scales. By using a coupling technique that bridges meso- and micro-scales, high-resolution nested Large-Eddy Simulations can be dynamically informed by large-scale numerical weather prediction models, resulting in more accurate and reliable simulations of the planetary boundary layer. This approach has numerous beneficial applications, including the wind energy sector. However, given the inherent complexity of expensive multiscale simulations, particularly in areas of complex terrain, numerous assumptions and fine tuning are required to produce accurate output that is of practical importance. Assessing the relative importance of a set of input assumptions for wind energy applications is the main focus of the present study.

Specifically, we analyze a recent dataset of multiscale WRF simulations [39] to investigate the sensitivity of wind power simulations to different input factors in the innermost domain. Both time-averaged estimates and time-resolved series are investigated, of both wind speed at hub height and power production, through four-way ANOVAs. Simulations cover a four-day long, precipitation-free springtime period and are centered over an area of complex terrain in central Portugal, Perdigão.

First, the analyses presented in this work show significant discrepancies in wind speed estimates with multiscale simulations, that lead to even more considerable variations in wind power calculations. In particular, this variability is stronger over the ridges and in the in-between valley. For a 2 MW wind turbine located on the South-West ridge, we

find that the ensemble average power production predicted by multiscale simulations is 840 kW for a four-day time average (capacity factor of 0.42), and that the interquartile range across the ensemble members is approximately 250 kW. In other words, the 75th percentile estimate predicts that up to approximately 850 standard American households (1.2 kW/household, per day) could be powered by one single 2 MW wind turbine, whereas the 25th percentile estimate predicts that about 625 households could be powered (assuming to perfectly match the load). When scaling up these findings for an entire wind farm, the variations among simulations can become significant for real-world wind energy challenges. While there is strong potential for multiscale simulations to fill in gaps in estimating wind energy resources, there is a need of targeting this uncertainty to make multiscale tools fully operational for wind energy purposes.

We further analyze the main factors that explain such uncertainty in multiscale calculations, to inform future research directions. First, we find that most of the ensemble discrepancies occur during day-to-night transitions and synoptic transitions. Variance decomposition demonstrates that the resolution of topography and land use dataset are the primary factor of such variability. However, under specific periods of time (i.e., synoptic and day–night transitions) simulations are also sensitive to other factors, as mesoscale LBCs and modeling turbulence in the gray zone, which can locally overtake topography. The model appears insensitive to how the sub-grid scale is modeled in the innermost domain, somewhat differently from what found in idealized studies [70]. In other words, other factors relevant in realistic simulations appear to be more important than the SGS model in predicting hub-height wind speed with multiscale simulations. Furthermore, in the deepest region of the valley, the topography factor is the major driver of variability within the ensemble, regardless of the sub-period analyzed, given the large differences in the WRF default datasets and the ad-hoc high-resolution ones at 30 m resolutions.
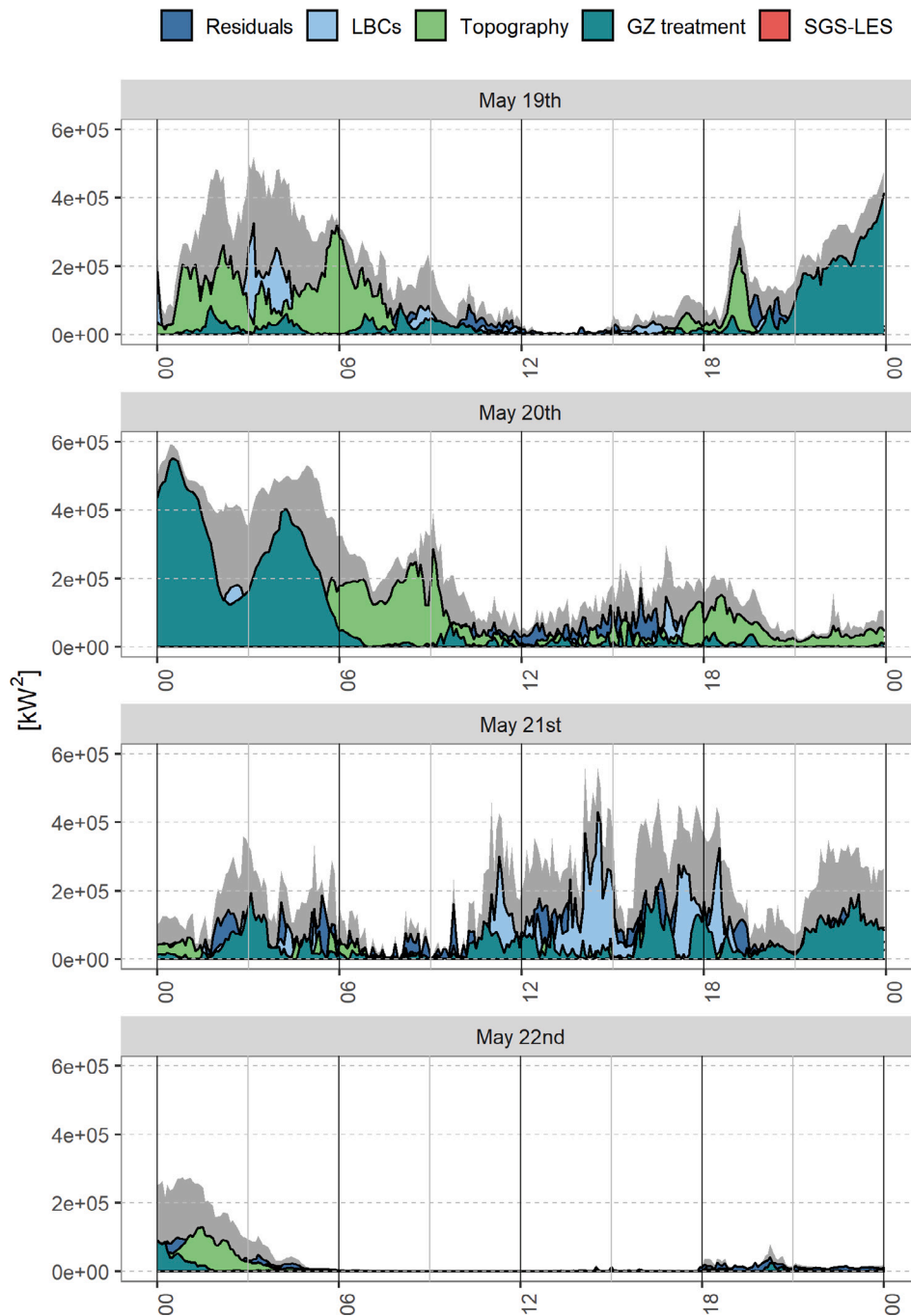
Fig. 12. Decomposition of total variance [kW^2] of wind power at 78 m above ground at the turbine site on each simulated day. The total variance is reported in gray.

Decomposition of variance performed on high-resolution temporal data (five-minutes) over the whole time series at the turbine site indicates strong inter-daily variability, and a coherent and recurrent daily pattern is not found. Occasionally, individual factors can persistently prevail over the others for certain time frames, in driving the overall ensemble spread. In summary, when conducting a time-averaged analysis for applications such as optimal turbine placement and studying regional climatology, special care should be taken in selecting appropriate topography and land use datasets, because they have a large effect on the long-term *time-averaged* wind speed. On the other hand, for short-term forecasts of wind power, such as those one needed for energy market applications, it appears that the way that turbulence is modeled across scales can have significant impacts on the final wind power forecasts. It is important to acknowledge that our

findings pertain specifically to our model setup at the Perdigão field site, for the four days considered. Nevertheless, they provide valuable insights into understanding the sensitivity of realistic multiscale experiments conducted in complex terrain and shed light on the underlying mechanisms driving this sensitivity for wind energy estimates.

Given the high computational cost of performing full-physics coupled meso- to micro-scale simulations (as reported in [39]), we are constrained to test the model's sensitivity to only a limited set of factors. It remains of interest to consider further initial parameters and assumptions, including the role of canopy and grid spacing, which may also influence predictions. Several authors [41,71] have argued that the parameterization of forest canopy directly in the momentum equations are critical to correctly recreate flow dynamics in the Perdigão domain. Future sensitivity studies may thus focus on assessing how sensitive

the model is to the adopted canopy model and its relative importance compared to other modeling choices that real multiscale problems require. Future work may also be directed to perform a comprehensive evaluation of model's skill against a range of observations for multiple variables and resolutions, that will inform on best model practices.

Financial disclosure

CRediT authorship contribution statement

Giorgia De Moliner: Writing – review & editing, Writing – original draft, Visualization, Validation, Software, Methodology, Investigation, Formal analysis, Data curation. **Paolo Giani:** Writing – review & editing, Writing – original draft, Validation, Software, Methodology, Investigation, Data curation, Conceptualization. **Giovanni Lonati:** Writing – review & editing, Supervision, Project administration, Conceptualization. **Paola Crippa:** Conceptualization, Funding acquisition, Methodology, Project administration, Resources, Supervision, Writing – original draft, Writing – review & editing.

Declaration of competing interest

The authors declare that they have no known competing financial interests or personal relationships that could have appeared to influence the work reported in this paper.

Data availability

Time-resolved wind data for the 36 simulations presented in this work are available at this repository https://github.com/Env-an-Stat-group/24.DeMoliner.APEN. Spatial data are available upon request. Quality controlled, preprocessed wind measurements were obtained from the NCAR/EOL repository, with permanent doi: 10.26023/ZDMJ-D1TY-FG14.

References

[1] European Commission. European green deal. 2020, https://ec.europa.eu/info/strategy/priorities-2019-2024/european-green-deal_en. [Accessed: 21 April 2023].
[2] National Development and Reform Commission of the People's Republic of China. Outline of the 14th five-year plan (2021–2025) for national economic and social development and the long-range objectives through the year 2035. 2021, http://www.gov.cn/zhengce/2021-03/11/content_5591362.htm. [Accessed: 21 April 2023].
[3] International Energy Agency. World energy outlook 2022. 2022, OECD/IEA, URL https://www.iea.org/reports/world-energy-outlook-2022. Accessed 21 April 21, 2023.
[4] Jacobson MZ, Delucchi MA. Providing all global energy with wind, water, and solar power, Part I: Technologies, energy resources, quantities and areas of infrastructure, and materials. Energy Policy 2011;39(3):1154–69. http://dx.doi.org/10.1016/j.enpol.2010.11.040.
[5] Jacobson MZ, Archer CL. Saturation wind power potential and its implications for wind energy. Proc Natl Acad Sci 2012;109(39):15679–84. http://dx.doi.org/10.1073/pnas.1208993109.
[6] Veers P, Dykes K, Lantz E, Barth S, Bottasso CL, Carlson O, et al. Grand challenges in the science of wind energy. Science 2019;366(6464). http://dx.doi.org/10.1126/science.aau2027.
[7] Dykes K, Hand M, Stehly T, Veers P, Robinson M, Lantz E, et al. Enabling the SMART wind power plant of the future through science-based innovation. Tech. rep., Golden, Colorado: National Renewable Energy Laboratory; 2017.
[8] Haupt SE, Kosovic B, Shaw W, Berg LK, Churchfield M, Cline J, et al. On bridging a modeling scale gap: Mesoscale to microscale coupling for wind energy. Bull Am Meteorol Soc 2019;100(12):2533–50.
[9] Lundquist KA, Chow FK, Lundquist JK. An immersed boundary method for the Weather Research and Forecasting model. Mon Weather Rev 2010;138(3):796–817.
[10] Jiménez-Esteve B, Udina M, Soler MR, Pepin N, Miró JR. Land use and topography influence in a complex terrain area: A high resolution mesoscale modelling study over the Eastern Pyrenees using the WRF model. Atmos Res 2018;202(November 2017):49–62. http://dx.doi.org/10.1016/j.atmosres.2017.11.012.
[11] Giani P, Genton MG, Crippa P. Modeling the convective boundary layer in the Terra Incognita: Evaluation of different strategies with real-case simulations. Mon Weather Rev 2022;150(5):981–1001.
[12] Haupt SE, Berg LK, Churchfield M, Kosović B, Mirocha J, Shaw W. Mesoscale to microscale coupling for wind energy applications: Addressing the challenges. J Phys Conf Ser 2020. http://dx.doi.org/10.1088/1742-6596/1452/1/012076.
[13] Wyngaard JC. Toward numerical modeling in the "Terra Incognita". J Atmos Sci 2004;61(14):1816–26.
[14] Zhou B, Simon JS, Chow FK. The convective boundary layer in the Terra Incognita. J Atmos Sci 2014;71(7):2545–63.
[15] Rai RK, Berg LK, Kosović B, Haupt SE, Mirocha JD, Ennis BL, et al. Evaluation of the impact of horizontal grid spacing in Terra Incognita on coupled mesoscale–microscale simulations using the WRF framework. Mon Weather Rev 2019;147(3):1007–27. http://dx.doi.org/10.1175/MWR-D-18-0282.1.
[16] Ching J, Rotunno R, LeMone M, Martilli A, Kosovic B, Jimenez PA, et al. Convectively induced secondary circulations in fine-grid mesoscale numerical weather prediction models. Mon Weather Rev 2014;142(9):3284–302.
[17] Zhang X, Bao J-W, Chen B, Grell ED. A three-dimensional scale-adaptive turbulent kinetic energy scheme in the WRF-ARW model. Mon Weather Rev 2018;146(7):2023–45.
[18] Ito J, Niino H, Nakanishi M, Moeng C-H. An extension of the Mellor–Yamada model to the Terra Incognita zone for dry convective mixed layers in the free convection regime. Bound-Layer Meteorol 2015;157(1):23–43.
[19] Boutle IA, Eyre JEJ, Lock AP. Seamless stratocumulus simulation across the turbulent gray zone. Mon Weather Rev 2014;142(4):1655–68.
[20] Shin HH, Hong S-Y. Representation of the subgrid-scale turbulent transport in convective boundary layers at gray-zone resolutions. Mon Weather Rev 2015;143(1):250–71.
[21] Juliano TW, Kosović B, Jiménez PA, Eghdami M, Haupt SE, Martilli A. "Gray zone" simulations using a three-dimensional planetary boundary layer parameterization in the weather research and forecasting model. Mon Weather Rev 2021;150(7):1585–619. http://dx.doi.org/10.1175/mwr-d-21-0164.1.
[22] Talbot C, Bou-Zeid E, Smith J. Nested mesoscale large-eddy simulations with WRF: Performance in real test cases. J Hydrometeorol 2012;13(5):1421–41.
[23] Rai RK, Berg LK, Kosović B, Mirocha JD, Pekour MS, Shaw WJ. Comparison of measured and numerically simulated turbulence statistics in a convective boundary layer over complex terrain. Bound-Lay Meteorol 2017;163(1):69–89.
[24] Muñoz-Esparza D, Lundquist JK, Sauer JA, Kosović B, Linn RR. Coupled mesoscale-LES modeling of a diurnal cycle during the CWEX-13 field campaign: From weather to boundary-layer eddies. J Adv Modelling Earth Syst 2017;9(3):1572–94.
[25] Doubrawa P, Muñoz-Esparza D. Simulating real atmospheric boundary layers at gray-zone resolutions: How do currently available turbulence parameterizations perform? Atmosphere 2020;11(4):345.
[26] Dudhia J. Challenges in sub-kilometer grid modeling of the convective planetary boundary layer. Meteorology 2022;1:402–13. http://dx.doi.org/10.3390/meteorology1040026.
[27] Giani P, Tagle F, Genton MG, Castruccio S, Crippa P. Closing the gap between wind energy targets and implementation for emerging countries. Appl Energy 2020;269:115085.
[28] Vanderwende BJ, Kosovic B, Lundquist JK, Mirocha JD. Simulating effects of a wind-turbine array using LES and RANS. J Adv Modelling Earth Syst 2017;548–65. http://dx.doi.org/10.1002/2016MS000652.
[29] Mirocha J, Churchfield MJ, Muñoz-Esparza D, Rai RK, Feng Y, Kosović B, et al. Large-eddy simulation sensitivities to variations of configuration and forcing parameters in canonical boundary-layer flows for wind energy applications. Wind Energy Sci 2018;3(2):589–613.
[30] Wang Q, Luo K, Yuan R, Wang S, Fan J, Cen K. A multiscale numerical framework coupled with control strategies for simulating a wind farm in complex terrain. Energy 2020;203:117913. http://dx.doi.org/10.1016/j.energy.2020.117913.
[31] van Stratum BJH, van Heerwaarden CC, Vilà-Guerau de Arellano J. The benefits and challenges of downscaling a global reanalysis with doubly-periodic large-eddy simulations. J Adv Modelling Earth Syst 2023;15(10). http://dx.doi.org/10.1029/2023MS003750, e2023MS003750, URL https://agupubs.onlinelibrary.wiley.com/doi/abs/10.1029/2023MS003750.
[32] Gustafson WI, Vogelmann AM, Li Z, Cheng X, Dumas KK, Endo S, et al. The Large-Eddy Simulation (LES) Atmospheric Radiation Measurement (ARM) Symbiotic Simulation and Observation (LASSO) activity for continental shallow convection. Bull Am Meteorol Soc 2020;101(4):E462–79. http://dx.doi.org/10.1175/BAMS-D-19-0065.1.

[33] Arthur RS, Mirocha JD, Marjanovic N, Hirth BD, Schroeder JL, Wharton S, et al. Multi-scale simulation of wind farm performance during a frontal passage. Atmosphere 2020;11. http://dx.doi.org/10.3390/atmos11030245.

[34] Prósper MA, Otero-Casal C, Fernández FC, Miguez-Macho G. Wind power forecasting for a real onshore wind farm on complex terrain using WRF high resolution simulations. Renew Energy 2019;135:674–86. http://dx.doi.org/10.1016/j.renene.2018.12.047.

[35] Marjanovic N, Wharton S, Chow FK. Investigation of model parameters for high-resolution wind energy forecasting: Case studies over simple and complex terrain. J Wind Eng Ind Aerodyn 2014;134:10–24. http://dx.doi.org/10.1016/j.jweia.2014.08.007, URL http://dx.doi.org/10.1016/j.jweia.2014.08.007.

[36] Solbakken K, Birkelund Y. Evaluation of the Weather Research and Forecasting (WRF) model with respect to wind in complex terrain. J Phys Conf Ser 2018;1102. http://dx.doi.org/10.1088/1742-6596/1102/1/012011.

[37] Stieren A, Gadde SN, Stevens RJ. Modeling dynamic wind direction changes in large eddy simulations of wind farms. Renew Energy 2021;170:1342–52. http://dx.doi.org/10.1016/j.renene.2021.02.018.

[38] Shi J, Liu X, Li Y, Liu Y, Roux G, Shi L, et al. Wind speed forecasts of a mesoscale ensemble for large-scale wind farms in Northern China: Downscaling effect of global model forecasts. Energies 2022;15. http://dx.doi.org/10.3390/en15030896.

[39] Giani P, Crippa P. On the sensitivity of large eddy simulations of the atmospheric boundary layer coupled with realistic large scale dynamics. Mon Weather Rev 2024;152(4):1057 – 1075. http://dx.doi.org/10.1175/MWR-D-23-0101.1.

[40] Fernando HJ, Mann J, Palma JM, Lundquist JK, Barthelmie RJ, Belo-Pereira M, et al. The Perdigão: Peering into microscale details of mountain winds. Bull Am Meteorol Soc 2019;100(5):799–820. http://dx.doi.org/10.1175/BAMS-D-17-0227.1.

[41] Wagner J, Gerz T, Wildmann N, Gramitzky K. Long-term simulation of the boundary layer flow over the double-ridge site during the Perdigão 2017 field campaign. Atmos Chem Phys 2019;19(2):1129–46.

[42] Quimbayo-Duarte J, Wagner J, Wildmann N, Gerz T, Schmidli J. Evaluation of a forest parameterization to improve boundary layer flow simulations over complex terrain. A case study. Geosci Model Dev 2022;15:5195–209.

[43] Connolly A, van Veen L, Neher J, Geurts BJ, Mirocha J, Chow FK. Efficacy of the cell perturbation method in large-eddy simulations of boundary layer flow over complex terrain. Atmosphere 2021;12(1):1–28. http://dx.doi.org/10.3390/atmos12010055.

[44] Wise AS, Neher JMT, Arthur RS, Mirocha JD, Lundquist JK, Chow FK. Meso-to microscale modeling of atmospheric stability effects on wind turbine wake behavior in complex terrain. Wind Energy Sci 2022;7:367–86.

[45] Skamarock WC, Klemp JB, Dudhia JB, Gill DO, Barker DM, Duda MG, et al. A Description of the Advanced Research WRF Model Version 4.3. In: NCAR technical note. Tech. Rep. July, Boulder, Colorado: National Center for Atmospheric Research (NCAR); 2021, p. 1–165.

[46] Beck J, Brown J, Dudhia J, Gill D, Hertneky T, Klemp J, et al. An evaluation of a hybrid, terrain-following vertical coordinate in the WRF-based rap and HRRR models. Weather Forecast 2020;35(3):1081–96. http://dx.doi.org/10.1175/WAF-D-19-0146.1.

[47] Muñoz-Esparza D, Kosović B, Mirocha J, van Beeck J. Bridging the transition from mesoscale to microscale turbulence in numerical weather prediction models. Bound-Layer Meteorol 2014;153(3):409–40.

[48] Werner M. Shuttle Radar Topography Mission (SRTM) mission overview. Frequenz 2001;55:75–9.

[49] Pineda N, Jorba O, Jorge J, Baldasano JM. Using NOAA AVHRR and SPOT VGT data to estimate surface parameters: Application to a mesoscale meteorological model. Int J Remote Sens 2004;25(1):129–43. http://dx.doi.org/10.1080/0143116031000115201.

[50] NCEP. NCEP GDAS/FNL 0.25 degree global tropospheric analyses and forecast grids. Boulder CO: Research Data Archive at the National Center for Atmospheric Research, Computational and Information Systems Laboratory; 2015, http://dx.doi.org/10.5065/D65Q4T4Z, Online Dataset.

[51] European Centre for Medium-Range Weather Forecasts. ECMWF's operational model analysis, starting in 2011. 2011, http://dx.doi.org/10.5065/D6ZG6Q9F, Online Dataset.

[52] Hersbach H, Bell B, Berrisford P, Hirahara S, Horányi A, Muñoz-Sabater J, et al. The ERA5 global reanalysis. Q J R Meteorol Soc 2020;146(730):1999–2049. http://dx.doi.org/10.1002/qj.3803.

[53] Hong S-Y, Noh Y, Dudhia J. A new vertical diffusion package with an explicit treatment of entrainment processes. Mon Weather Rev 2006;134(9):2318–41.

[54] Deardorff JW. Stratocumulus-capped mixed layers derived from a three-dimensional model. Bound-Lay Meteorol 1980;18(4):495–527. http://dx.doi.org/10.1007/BF00119502.

[55] Smagorinsky J. General circulation experiments with the primitive equations: I. The basic experiment. Mon Weather Rev 1963;91(3):99–164.

[56] Lilly DK. The representation of small-scale turbulence in numerical simulation experiments. IBM Form 1967;195–210.

[57] Wilks DS. Statistical methods in the atmospheric sciences. Amsterdam; Boston: Elsevier Academic Press; 2011.

[58] Pierrot M. The wind power database. 2023, https://www.thewindpower.net/index.php. [Accessed: January 2023].

[59] Lee JCY, Fields MJ. An overview of wind-energy-production prediction bias, losses, and uncertainties. Wind Energy Sci 2021;6(2):311–65. http://dx.doi.org/10.5194/wes-6-311-2021, URL https://wes.copernicus.org/articles/6/311/2021/.

[60] Mirocha JD, Kosovic B, Aitken ML, Lundquist JK. Implementation of a generalized actuator disk wind turbine model into the weather research and forecasting model for large-eddy simulation applications. J Renew Sustain Energy 2014;6(1):013104. http://dx.doi.org/10.1063/1.4861061.

[61] Doyle JD, Gaberšek S, Jiang Q, Bernardet L, Brown JM, Dörnbrack A, et al. An intercomparison of T-REX mountain-wave simulations and implications for mesoscale predictability. Mon Weather Rev 2011;139(9):2811–31. http://dx.doi.org/10.1175/MWR-D-10-05042.1, URL https://journals.ametsoc.org/view/journals/mwre/139/9/mwr-d-10-05042.1.xml.

[62] Reinecke PA, Durran DR. Initial-condition sensitivities and the predictability of downslope winds. J Atmos Sci 2009;66(11):3401–18. http://dx.doi.org/10.1175/2009JAS3023.1, URL https://journals.ametsoc.org/view/journals/atsc/66/11/2009jas3023.1.xml.

[63] Schmidli J, Böing S, Fuhrer O. Accuracy of simulated diurnal valley winds in the swiss alps: Influence of grid resolution, topography filtering, and land surface datasets. Atmosphere 2018;9(5). http://dx.doi.org/10.3390/atmos9050196, URL https://www.mdpi.com/2073-4433/9/5/196.

[64] Lehner M, Rotach MW. Current challenges in understanding and predicting transport and exchange in the atmosphere over mountainous terrain. Atmosphere 2018;9(7). http://dx.doi.org/10.3390/atmos9070276, URL https://www.mdpi.com/2073-4433/9/7/276.

[65] Chow FK, Schär C, Ban N, Lundquist KA, Schlemmer L, Shi X. Crossing multiple gray zones in the transition from mesoscale to microscale simulation over complex terrain. Atmosphere 2019;10(5). http://dx.doi.org/10.3390/atmos10050274, URL https://www.mdpi.com/2073-4433/10/5/274.

[66] Liu Y, Liu Y, Muñoz-Esparza D, Hu F, Yan C, Miao S. Simulation of flow fields in complex terrain with WRF-LES: Sensitivity assessment of different PBL treatments. J Appl Meteorol Climatol 2020;59(9):1481–501.

[67] Dudhia J. Reply. Mon Weather Rev 1994;11–3.

[68] Durran DR, Klemp JB. A compressible model for the simulation of moist mountain waves. Mon Weather Rev 1983;111(12):2341–61.

[69] EIA. U.S. energy information administration, Residential Energy Consumption Survey (RECS). 2020, Online Dataset, URL https://www.eia.gov/consumption/residential/index.php.

[70] Ma Y, Liu H. Large-eddy simulations of atmospheric flows over complex terrain using the immersed-boundary method in the weather research and forecasting model. Bound-Lay Meteorol 2017;165(3):421–45. http://dx.doi.org/10.1007/s10546-017-0283-9.

[71] Venkatraman K, Hågbo T-O, Buckingham S, Giljarhus KET. Effect of different source terms and inflow direction in atmospheric boundary modeling over the complex terrain site of Perdigão. Wind Energy Sci 2023;8:85–108. http://dx.doi.org/10.5194/wes-8-85-2023.